AIAA AVIATION Forum
13-17 June 2016, Washington, D.C.
46th AIAA Fluid Dynamics Conference

AIAA 2016-3185

Simulation of Airfoil Stall Flows Using IDDES with High Order Schemes

Yunchao Yang * Gecheng Zha †
Dept. of Mechanical and Aerospace Engineering
University of Miami, Coral Gables, Florida 33124
E-mail: gzha@miami.edu

Abstract

The IDDES(Improved Delayed Detached Eddy Simulation) turbulence modeling is validated with the flat plate boundary layer and is used to investigate the stall flows of NACA0012 airfoil. The spatially filtered unsteady 3D Navier-Stokes equations are solved using a 5th order WENO reconstruction with a low diffusion E-CUSP scheme for the inviscid fluxes and a conservative 4th order central differencing for the viscous terms. Validation and comparison of flat plate boundary layer velocity profiles are conducted at different Mach numbers, Reynolds numbers and mesh sizes using the Spalart-Allmaras(S-A) URANS, DES97, DDES, and IDDES. The study indicates that the IDDES is accurate to predict the law of the wall regardless of the mesh size, whereas model stress depletion and log layer mismatch are observed in the DES97 and DDES computations.

Stalled flows of the NACA0012 at four different angle of attacks of $5°, 17°, 45°$, and $60°$ are simulated to investigate the capability of the URANS, DDES, and IDDES to resolve massive separated flows. At high angle of attack(AoAs), the lift and drag coefficients calculated by IDDES are much more accurate than those of the URANS computation with S-A turbulence model. The S-A URANS simulation over-predicts the drag coefficient by about 30%, whereas the IDDES accurately predicts the drag coefficient. For the massive separated flows, more realistic flow structures are resolved by the IDDES simulation.

1 Introduction

Airfoil stall flows at high angle of attack with massive flow separation are very challenging to simulate accurately[1]. Large vortex structures are formed around the airfoil leading edge and travel along the airfoil suction surface as they grow, and get separated from the airfoil surface near the trailing edge.

Reynolds-averaged Navier-Strokes (RANS) methods are not appropriate for simulating stalled vortical flow structures due to its universal scale filtering. As an alternative, large eddy simulation (LES) is developed to directly simulate the large flow structures and model the small eddy structures that are more isotropic. However, LES is much more CPU expensive. The hybrid RANS/LES approach is a promising compromise for engineering applications by taking the advantages of RANS's high efficiency and LES's high accuracy with more affordable computational cost.

The detached eddy simulation (DES, or DES97) is the first and most popular non-zonal hybrid RANS/LES strategy suggested by Spalart et al. in 1997[2]. Near the solid surface within the wall boundary layer, the

* Ph.D. Candidate, AIAA student member
† Professor, ASME Fellow, AIAA associate Fellow

unsteady RANS(URANS) turbulence modeling is utilized. Away from the boundary layer, the DES97 model is automatically converted to LES. The Delayed detached-eddy simulation (DDES) suggested by Spalart et al. [3] is improved to resolve model stress depletion(MSD) and grid induced separation(GIS) problems. The more recently improved DDES(IDDES) model is formulated by Travin et al.[4] and Shur et al.[5] by coupling wall-modeled LES(WMLES) and DDES to eliminate the log layer mismatch(LLM) problem, and maintain the compatibility with the general DES approach. The major improvement of IDDES can be summarized as a near-wall modification of the LES filter Δ, and a more rapid transition between the RANS and LES length scales than DES97 or DDES. The IDDES method utilizes more sensors in the boundary layer region and a new blending function based on theoretical considerations and empirical tuning[6].

Computational simulations of airfoil stall flows have been conducted extensively by various researchers[4, 7, 8, 9]. Travin et al.[4] simulate the massively separated flows over airfoil, and observe that the DDES performs similar to the original DES97 for their cases. Morton et al.[7] employed DES97 to simulate a full F/A-18E aircraft experiencing massively separated flows with good agreement with the experiment. Durrani et al. [8] applied DES97 and DDES to simulate the flow around the A-airfoil at the maximum lift condition(AoA=13.3°). They observed that for the flow with a relatively thick boundary layer and a mild trailing-edge separation, DES97 performs better than DDES due to its relatively lower turbulence dissipation levels.

The objective of this paper are two-folds: 1) Apply the high order accuracy schemes to IDDES with different mesh sizes to demonstrate their performance at different conditions; 2) Compare the IDDES turbulence modeling with advantages over RANS model and DDES for airfoil stalled flows.

2 Numerical Methodology

2.1 Governing Equations

The filtered 3D Navier-Stokes governing equations in generalized coordinates are expressed as:

$$\frac{\partial \mathbf{Q}}{\partial t} + \frac{\partial \mathbf{E}}{\partial \xi} + \frac{\partial \mathbf{F}}{\partial \eta} + \frac{\partial \mathbf{G}}{\partial \zeta} = \frac{1}{Re}\left(\frac{\partial \mathbf{E}_v}{\partial \xi} + \frac{\partial \mathbf{F}_v}{\partial \eta} + \frac{\partial \mathbf{G}_v}{\partial \zeta} + \mathbf{S}\right) \tag{1}$$

where Re is the Reynolds number. The equations are nondimenisonalized based on airfoil chord L_∞, freestream density ρ_∞ and velocity U_∞.

The conservative variable vector $\mathbf{Q}$, the inviscid flux vectors $\mathbf{E}$, $\mathbf{F}$, $\mathbf{G}$, the viscous flux $\mathbf{E_v}$, $\mathbf{F_v}$, $\mathbf{G_v}$ and the source term vector $\mathbf{S}$ are expressed as

$$\mathbf{Q} = \frac{1}{J}\begin{pmatrix} \bar\rho \\ \bar\rho\tilde u \\ \bar\rho\tilde v \\ \bar\rho\tilde w \\ \bar\rho\tilde e \\ \bar\rho\tilde\nu_t \end{pmatrix}, \mathbf{E} = \begin{pmatrix} \bar\rho U \\ \bar\rho\tilde u U + l_x\bar p \\ \bar\rho\tilde v U + l_y\bar p \\ \bar\rho\tilde w U + l_z\bar p \\ (\bar\rho\tilde e + \bar p)\,U - l_t\bar p \\ \bar\rho\tilde\nu U \end{pmatrix}, \mathbf{F} = \begin{pmatrix} \bar\rho V \\ \bar\rho\tilde u V + m_x\bar p \\ \bar\rho\tilde v V + m_y\bar p \\ \bar\rho\tilde w V + m_z\bar p \\ (\bar\rho\tilde e + \bar p)\,V - m_t\bar p \\ \bar\rho\tilde\nu V \end{pmatrix}, \mathbf{G} = \begin{pmatrix} \bar\rho W \\ \bar\rho\tilde u W + n_x\bar p \\ \bar\rho\tilde v W + n_y\bar p \\ \bar\rho\tilde w W + n_z\bar p \\ (\bar\rho\tilde e + \bar p)\,W - n_t\bar p \\ \bar\rho\tilde\nu W \end{pmatrix} \tag{2}$$

$$\mathbf{E_v} = \begin{pmatrix} 0 \\ l_k\bar\tau_{xk} \\ l_k\bar\tau_{yk} \\ l_k\bar\tau_{zk} \\ l_k\left(\tilde u_i\bar\tau_{ki} - \bar q_k\right) \\ \frac{\bar\rho}{\sigma}\left(\nu+\tilde\nu\right)\left(\mathbf{l}\bullet\nabla\tilde\nu\right) \end{pmatrix}, \mathbf{F_v} = \begin{pmatrix} 0 \\ m_k\bar\tau u_{xk} \\ m_k\bar\tau_{yk} \\ m_k\bar\tau u_{zk} \\ m_k\left(\tilde u_i\bar\tau_{ki} - \bar q_k\right) \\ \frac{\bar\rho}{\sigma}\left(\nu+\tilde\nu\right)\left(\mathbf{m}\bullet\nabla\tilde\nu\right) \end{pmatrix}, \mathbf{G_v} = \begin{pmatrix} 0 \\ n_k\bar\tau_{xk} \\ n_k\bar\tau_{yk} \\ n_k\bar\tau_{zk} \\ n_k\left(\tilde u_i\bar\tau_{ki} - \bar q_k\right) \\ \frac{\bar\rho}{\sigma}\left(\nu+\tilde\nu\right)\left(\mathbf{n}\bullet\nabla\tilde\nu\right) \end{pmatrix} \tag{3}$$

$$\mathbf{S} = \frac{1}{J}\begin{pmatrix} 0 \\ 0 \\ 0 \\ 0 \\ 0 \\ S_\nu \end{pmatrix} \tag{4}$$

where ρ is the density, p is the static pressure, and e is the total energy per unit mass. The overbar term denotes a regular filtered variable in the LES region,or a Reynolds-averaged value in the RANS region. And the tilde symbol is used to denote the Favre filtered variable. ν is kinematic viscosity and $\tilde{\nu}$ is the working variable related to eddy viscosity in S-A and IDDES turbulence one equation model[10]. U, V and W are the contravariant velocities in ξ, η, ζ directions, and defined as

$$\begin{aligned} U &= l_t + \mathbf{l} \bullet \mathbf{V} = l_t + l_x\tilde{u} + l_y\tilde{v} + l_z\tilde{w} \\ V &= m_t + \mathbf{m} \bullet \mathbf{V} = m_t + m_x\tilde{u} + m_y\tilde{v} + m_z\tilde{w} \\ W &= n_t + \mathbf{n} \bullet \mathbf{V} = n_t + n_x\tilde{u} + n_y\tilde{v} + n_z\tilde{w} \end{aligned} \tag{5}$$

where J is the Jacobian of the coordinate transformation. l_t, m_t and n_t are the components of the interface contravariant velocity of the grid in ξ, η and ζ directions respectively. $\mathbf{l}$, $\mathbf{m}$ and $\mathbf{n}$ denote the normal vectors located at the centers of ξ, η and ζ interfaces of the control volume with their magnitudes equal to the surface areas and pointing to the directions of increasing ξ, η and ζ.

$$\mathbf{l} = \frac{\nabla\xi}{J},\ \mathbf{m} = \frac{\nabla\eta}{J},\ \mathbf{n} = \frac{\nabla\zeta}{J} \tag{6}$$

$$l_t = \frac{\xi_t}{J},\ m_t = \frac{\eta_t}{J},\ n_t = \frac{\zeta_t}{J} \tag{7}$$

In the generalized coordinates, $\Delta\xi = \Delta\eta = \Delta\zeta = 1$. Since the DES-family approach is based on S-A model, the formulations of the original S-A model are give below. The source term S_ν from the S-A model in Eq. (4), is given by

$$\begin{aligned} S_\nu = \bar{\rho}C_{b1}\left(1 - f_{t2}\right)\tilde{S}\tilde{\nu} + \tfrac{1}{Re}\Big[-\bar{\rho}\left(C_{w1}f_w - \tfrac{C_{b1}}{\kappa^2}f_{t2}\right)\left(\tfrac{\tilde{\nu}}{d}\right)^2 \\ + \tfrac{\bar{\rho}}{\sigma}C_{b2}\left(\nabla\tilde{\nu}\right)^2 - \tfrac{1}{\sigma}\left(\nu + \tilde{\nu}\right)\nabla\tilde{\nu} \bullet \nabla\bar{\rho}\Big] + Re\left[\bar{\rho}f_{t1}\left(\Delta q\right)^2\right] \end{aligned} \tag{8}$$

where

$$\chi = \frac{\tilde{\nu}}{\nu}, \qquad f_{v1} = \frac{\chi^3}{\chi^3 + c_{v1}^3}, \qquad f_{v2} = 1 - \frac{\chi}{1 + \chi f_{v1}}, \qquad f_{t1} = C_{t1}g_t exp\left[-C_{t2}\frac{\omega_t^2}{\Delta U^2}\left(d^2 + g_t^2 d_t^2\right)\right] \tag{9}$$

$$f_{t2} = C_{t3}exp\left(-C_{t4}\chi^2\right), \qquad f_w = g\left(\frac{1 + c_{w3}^6}{g^6 + c_{w3}^6}\right)^{1/6}, \qquad g = r + c_{w2}(r^6 - r) \tag{10}$$

$$g_t = min\left(0.1, \frac{\Delta q}{\omega_t \Delta x_t}\right), \qquad \tilde{S} = S + \frac{\tilde{\nu}}{k^2 d^2 R_e}f_{v2}, \qquad r = \frac{\tilde{\nu}}{\tilde{S}k^2 d^2 R_e} \tag{11}$$

where, ω_t is the wall vorticity at the wall boundary layer trip location, d is the distance to the closest wall, d_t is the distance of the field point to the trip location, Δq is the difference of the velocities between the field point and the trip location, Δx_t is the grid spacing along the wall at the trip location. The values of the coefficients are: $c_{b1} = 0.1355, c_{b2} = 0.622, \sigma = \frac{2}{3}, c_{w1} = \frac{c_{b1}}{k^2} + (1 + c_{b2})/\sigma, c_{w2} = 0.3, c_{w3} = 2, k = 0.41, c_{v1} = 7.1, c_{t1} = 1.0, c_{t2} = 2.0, c_{t3} = 1.1, c_{t4} = 2.0$.

The shear stress $\bar{\tau}_{ik}$ and total heat flux $\bar{q}_k$ in Cartesian coordinates is given by

$$\bar{\tau}_{ik} = (\mu + \mu_{DES})\left[\left(\frac{\partial\tilde{u}_i}{\partial x_k} + \frac{\partial\tilde{u}_k}{\partial x_i}\right) - \frac{2}{3}\delta_{ik}\frac{\partial\tilde{u}_j}{\partial x_j}\right] \tag{12}$$

$$\bar{q}_k = -\left(\frac{\mu}{Pr} + \frac{\mu_{DES}}{Pr_t}\right)\frac{\partial\tilde{T}}{\partial x_k} \tag{13}$$

where μ is from Sutherland's law. For DES approach in general, the eddy viscosity is represented by $\mu_{DES}(= \bar{\rho}\tilde{\nu}f_{v1})$.

2.2 Improved Delayed Detached Eddy Simulation(IDDES)

2.2.1 DES97

For the origianl DES97 model, a modification of a S-A RANS model is made to switch the model to a subgrid scale formulation in regions for LES calculations. The coefficients c_{t1} and c_{t3} in the S-A model are set to zero and the distance to the nearest wall, d, is replaced by $\tilde{d}$ as

$$\tilde{d} = min(d, C_{DES}\Delta) \tag{14}$$

2.2.2 DDES

The DDES model is suggested by Spalart et al. [3] to overcome the modeled stress depletion (MSD) for ambiguous grids. The DDES redefines the distance scale transition from RANS mode to LES mode $\tilde{d}$. The mechanism was identified as an encroachment of the RANS-LES interface inside the boundary layer, giving rise to reduced level of eddy viscosity on the LES-mode side.

$$\tilde{d} = d - f_d max(0, d - C_{DES}\Delta) \tag{15}$$

where

$$f_d = 1 - tanh([8r_d]^3) \tag{16}$$

$$r_d = \frac{\nu_t + \nu}{(U_{i,j}U_{i,j})^{0.5}k^2d^2R_e} \tag{17}$$

$$U_{i,j} = \frac{\partial u_i}{\partial x_j} \tag{18}$$

where Δ is the local grid filter scale, $U_{i,j}$ is the velocity gradient, and k denotes the Karmann constant.

2.2.3 IDDES

The Improved DDES(IDDES) is introduced by extending the DDES with the WMLES capacity. The IDDES has two branches, DDES and WMLES, including a set of empirical functions of subgrid length-scales designed to achieve good performance from these branches themselves and their coupling. By switching the activation of RANS and LES in different flow regions, IDDES significantly expands the scope of application of DDES with well-balanced and powerful numerical approach to complex turbulent flows at high Reynolds numbers.

The three aspects of IDDES are presented below: the DDES branch , the WMLES branch and hybridization of DDES and WMLES.

DDES branch of IDDES

This branch is responsible for the DDES-like functionality of IDDES and should become active only when the inflow conditions do not have any turbulent content (if a simulation has spatial periodicity, the initial conditions rather than the inflow conditions set the characteristics of the simulation), in particular when a grid of "boundary-layer type" precludes the resolution of the dominant eddies. The DDES formulation from Eq.(15) can be reformulated as

$$l_{DDES} = l_{RANS} - f_d max\{0, l_{RANS} - l_{LES}) \tag{19}$$

where the delaying function, f_d, is defined the same as

$$f_d = 1 - tanh[(8r_d)^3] \tag{20}$$

and the quantity r_d borrowed from the S-A RANS turbulence model:

$$r_d = \frac{\nu_t + \nu}{k^2 d_w^2 max[(U_{i,j}U_{i,j})^{0.5}, 10^{-10}]} \tag{21}$$

is a marker of the wall region, which is equal to 1 in a log layer and 0 in a free shear flow.

In Eq. (21), $U_{i,j}$ represents the velocity gradient, and k denotes the Karmann constant. Based on the general DES concept, in order to create a seamless hybrid model, the length-scale IDDES defined by Eq.19 is substituted into the background RANS model to replace the RANS length-scale, l_{RANS}, which is explicitly or implicitly involved in any such model. For instance, for the S-A model the length-scale is equal to the distance to the wall $l_{RANS} = d_w$. In the original DES97, the length-scale depends only on the local grid. In DDES and IDDES, it also depends on the solution of Eq. (19) and (21).

As far as the LES length-scale, l_{LES}, in Eq. (19) is concerned, it is defined via the subgrid length-scale as

$$l_{LES} = C_{DES}\Phi\Delta \tag{22}$$

where C_{DES} is the fundamental empirical constant of DES, 0.65. Φ is a low-Reynolds number correction introduced in order to compensate the activation of the low-Reynolds number terms of some background RANS model in LES mode. Both C_{DES} and Φ depend on the background RANS model, and Ψ is equal to 1 if the RANS model does not include any low-Reynolds number terms.

WMLES branch of IDDES

This branch is intended to be active only when the inflow conditions used in the simulation are unsteady and impose some turbulent content with the grid fine enough to resolve boundary-layer dominant eddies. It presents a new seamless hybrid RANS-LES model, which couples RANS and LES approaches via the introduction of the following blended RANS-LES length-scale:

$$l_{WMLES} = f_B(1 + f_e)l_{RANS} + (1 - f_B)l_{LES} \tag{23}$$

The empirical blending-function f_B depends upon d_w/h_{max} and is defined as

$$f_B = min\{2exp(-9\alpha^2), 1.0\}, \alpha = 0.25 - d_w/h_{max} \tag{24}$$

It varies from 0 to 1 and provides rapid switching of the model from RANS mode ($f_B = 1.0$) to LES mode ($f_B = 0$) within the range of wall distance $0.5h_{max} < d_w < h_{max}$

The second empirical function involved in Eq. (23), elevating-function, f_e, is aimed at preventing the excessive reduction of the RANS Reynolds stresses observed in the interaction of the RANS and LES regions in the vicinity of their interface. It is intended to eliminating the log-layer mismatch(LLM) problem.

$$f_e = max\{(f_{e1} - 1), 0\}\Phi f_{e2} \tag{25}$$

where the function f_{e1} is defined as

$$f_{e1}(d_w/h_{max}) = \begin{cases} 2exp(-11.09\alpha^2) & \text{if } \alpha \geq 0 \\ 2exp(-9.0\alpha^2) & \text{if } \alpha < 0 \end{cases} \tag{26}$$

It provides a grid-dependent "elevating"device for the RANS component of the WMLES length-scale.

The function f_{e2} is:

$$f_{e2} = 1.0 - max\{f_t, f_l\} \tag{27}$$

Blending DDES and WMLES branches

The DDES length-scale defined by Eq. (19) and that of the WMLES-branch defined by Eq. (23) do not blend directly in a way to ensure an automatic choice of the WMLES or DDES mode by the combined model, depending on the type of the simulation (with or without turbulent content) and the grid used.

However a modified version of equivalent length scale combination, namely,

$$\tilde{l}_{DDES} = \tilde{f}_d l_{RANS} + (1 - \tilde{f}_d)l_{LES} \tag{28}$$

where the blending function $\tilde{f}_d$ is defined by

$$\tilde{f}_d = max\{(1 - f_{dt}), f_B\} \tag{29}$$

with $f_{dt} = 1 - tanh[(8r_{dt})^3]$

With the use of Eq. (28), the required IDDES length-scale combining the DDES and WMLES length scales defined by Eq. (28) and (23) is straightforward and can be implemented as

$$l_{hyb} = \tilde{f}_d(1 + f_e)l_{RANS} + (1 - \tilde{f}_d)l_{LES} \tag{30}$$

With inflow turbulent content, f_{dt} is close to 1.0, $\tilde{f}_d$ is equal to f_B, so Eq. (30) is reducted to $l_{hyb} = l_{WMLES}$ in Eq. (23). Otherwise, f_e is zero, Eq. (30) is interpreted as $l_{hyb} = l_{DDES}$ in Eq. (28)

2.3 Time Marching Scheme

Following the dual time stepping method suggested by Jameson[11], an implicit pseudo time marching scheme using line Gauss-Seidel line relaxation is employed to solve the governing equations, as the following:

$$\frac{\partial \mathbf{Q}}{\partial t} = \frac{\mathbf{3Q^{n+1} - 4Q^n + Q^{n-1}}}{2\Delta t} \tag{31}$$

where $n-1$, n and $n+1$ are three sequential time levels, which have a time interval of Δt. The first-order Euler scheme is used to discretize the pseudo temporal term. The semi-discretized equations of the governing equations are given as the following:

$$\begin{gathered}\left[\left(\frac{1}{\Delta\widehat{\tau}} + \frac{1.5}{\Delta t}\right)I - \left(\frac{\partial R}{\partial \mathbf{Q}}\right)^{n+1,m}\right]\delta\mathbf{Q^{n+1,m+1}} \\ = R^{n+1,m} - \frac{\mathbf{3Q^{n+1,m} - 4Q^n + Q^{n-1}}}{2\Delta t}\end{gathered} \tag{32}$$

where the $\Delta\widehat{\tau}$ is the pseudo time step, and R stands for the net flux determined by the spatial high order numerical scheme, m is the iteration index for the pseudo time.

2.4 The Low Diffusion E-CUSP Scheme

The Low Diffusion E-CUSP(LDE) Scheme[12] is employed to calculate the inviscid fluxes. The key concept of LDE scheme is to split the inviscid flux into convective E^c and a pressure E^p based on characteristics analysis. In generalized coordinate system, the flux $\mathbf{E}$ can be split as the following:

$$\mathbf{E}' = E^c + E^p = \begin{pmatrix} \rho U \\ \rho u U \\ \rho v U \\ \rho w U \\ \rho e U \\ \rho\tilde{\nu} U \end{pmatrix} + \begin{pmatrix} 0 \\ \xi_x p \\ \xi_y p \\ \xi_z p \\ p\overline{U} \\ 0 \end{pmatrix} \tag{33}$$

where, U is the contravariant velocity as defined in Eq. (5). $\overline{U}$ is defined as:

$$\overline{U} = U - \xi_t = \xi_x u + \xi_y v + \xi_z w \tag{34}$$

The convective flux, E^c is evaluated by

$$E^c = \rho U \begin{pmatrix} 1 \\ u \\ v \\ w \\ e \\ \tilde{\nu} \end{pmatrix} = \rho U f^c,\ f^c = \begin{pmatrix} 1 \\ u \\ v \\ w \\ e \\ \tilde{\nu} \end{pmatrix} \tag{35}$$

Let

$$C = c\left(\xi_x^2 + \xi_y^2 + \xi_z^2\right)^{\frac{1}{2}} \tag{36}$$

where $c = \sqrt{\gamma RT}$ is the speed of sound. Then the convective flux at interface $i + \frac{1}{2}$ is evaluated as:

$$E^c_{i+\frac{1}{2}} = C_{\frac{1}{2}} \left[\rho_L C^+ f^c_L + \rho_R C^- f^c_R \right] \tag{37}$$

where, the subscripts L and R represent the left and right hand sides of the interface. The Mach number splitting of Edwards[13] is borrowed to determine C^+ and C^- as the following:

$$C_{\frac{1}{2}} = \frac{1}{2} \left(C_L + C_R \right) \tag{38}$$

$$C^+ = \alpha^+_L \left(1 + \beta_L \right) M_L - \beta_L M^+_L - M^+_{\frac{1}{2}} \tag{39}$$

$$C^- = \alpha^-_R \left(1 + \beta_R \right) M_R - \beta_R M^-_R + M^-_{\frac{1}{2}} \tag{40}$$

$$M_L = \frac{U_L}{C_{\frac{1}{2}}}, \; M_R = \frac{U_R}{C_{\frac{1}{2}}} \tag{41}$$

$$\alpha_{L,R} = \frac{1}{2} \left[1 \pm sign \left(M_{L,R} \right) \right] \tag{42}$$

$$\beta_{L,R} = -max \left[0, 1 - int \left(|M_{L,R}| \right) \right] \tag{43}$$

$$M^+_{\frac{1}{2}} = M_{\frac{1}{2}} \frac{C_R + C_L \Phi}{C_R + C_L} \tag{44}$$

$$M^-_{\frac{1}{2}} = M_{\frac{1}{2}} \frac{C_L + C_R \Phi^{-1}}{C_R + C_L} \tag{45}$$

$$\Phi = \frac{\left(\rho C^2 \right)_R}{\left(\rho C^2 \right)_L} \tag{46}$$

$$M_{\frac{1}{2}} = \beta_L \delta^+ M^-_L - \beta_R \delta^- M^+_R \tag{47}$$

$$M^\pm_{L,R} = \pm \frac{1}{4} \left(M_{L,R} \pm 1 \right)^2 \tag{48}$$

$$\delta^\pm = \frac{1}{2} \left\{ 1 \pm sign \left[\frac{1}{2} \left(M_L + M_R \right) \right] \right\} \tag{49}$$

The pressure flux, E^p is evaluated as the following

$$E^p_{i+\frac{1}{2}} = \begin{pmatrix} 0 \\ \mathcal{P}^+ p\, \xi_x \\ \mathcal{P}^+ p\, \xi_y \\ \mathcal{P}^+ p\, \xi_z \\ \frac{1}{2} p \left[\overline{U} + \overline{C}_{\frac{1}{2}} \right] \\ 0 \end{pmatrix}_L + \begin{pmatrix} 0 \\ \mathcal{P}^- p\, \xi_x \\ \mathcal{P}^- p\, \xi_y \\ \mathcal{P}^- p\, \xi_z \\ \frac{1}{2} p \left[\overline{U} - \overline{C}_{\frac{1}{2}} \right] \\ 0 \end{pmatrix}_R \tag{50}$$

The contravariant speed of sound $\overline{C}$ in the pressure vector is consistent with $\overline{U}$. It is computed based on C as the following,

$$\overline{C} = C - \xi_t \tag{51}$$

The use of $\overline{U}$ and $\overline{C}$ instead of U and C in the pressure vector is to take into account of the grid speed so that the flux will transit from subsonic to supersonic smoothly. When the grid is stationary, $\xi_t = 0$, $\overline{C} = C$, $\overline{U} = U$. The pressure splitting coefficient is:

$$\mathcal{P}^\pm_{L,R} = \frac{1}{4} \left(M_{L,R} \pm 1 \right)^2 \left(2 \mp M_L \right) \tag{52}$$

The LDE scheme can capture crisp shock profile and exact contact surface discontinuities as accurately as the Roe scheme[12].

2.5 The 5th Order WENO Scheme

For reconstruction of the interface flux, $E_{i+\frac{1}{2}} = E(Q_L, Q_R)$, the conservative variables Q_L and Q_R are evaluated by using the 5th order WENO scheme[14, 15]. For example,

$$(Q_L)_{i+\frac{1}{2}} = \omega_0 q_0 + \omega_1 q_1 + \omega_2 q_2 \tag{53}$$

where

$$q_0 = \frac{1}{3}Q_{i-2} - \frac{7}{6}Q_{i-1} + \frac{11}{6}Q_i \tag{54}$$

$$q_1 = -\frac{1}{6}Q_{i-1} + \frac{5}{6}Q_i + \frac{1}{3}Q_{i+1} \tag{55}$$

$$q_2 = \frac{1}{3}Q_i + \frac{5}{6}Q_{i+1} - \frac{1}{6}Q_{i+2} \tag{56}$$

$$\omega_k = \frac{\alpha_k}{\alpha_0 + \ldots + \alpha_{r-1}} \tag{57}$$

$$\alpha_k = \frac{C_k}{\epsilon + IS_k},\ k = 0, \ldots, r-1 \tag{58}$$

$$C_0 = 0.1,\ C_1 = 0.6,\ C_2 = 0.3 \tag{59}$$

$$IS_0 = \frac{13}{12}\left(Q_{i-2} - 2Q_{i-1} + Q_i\right)^2 + \frac{1}{4}\left(Q_{i-2} - 4Q_{i-1} + 3Q_i\right)^2 \tag{60}$$

$$IS_1 = \frac{13}{12}\left(Q_{i-1} - 2Q_i + Q_{i+1}\right)^2 + \frac{1}{4}\left(Q_{i-1} - Q_{i+1}\right)^2 \tag{61}$$

$$IS_2 = \frac{13}{12}\left(Q_i - 2Q_{i+1} + Q_{i+2}\right)^2 + \frac{1}{4}\left(3Q_i - 4Q_{i+1} + Q_{i+2}\right)^2 \tag{62}$$

ϵ is originally introduced to avoid the denominator becoming zero and is supposed to be a very small number. In [15], it is observed that IS_k will oscillate if ϵ is too small and also shift the weights away from the optimal values in the smooth region. The higher the ϵ values, the closer the weights approach the optimal values, C_k, which will give the symmetric evaluation of the interface flux with minimum numerical dissipation. When there are shocks in the flow field, ϵ can not be too large to maintain the sensitivity to shocks. In [15], $\epsilon = 10^{-2}$ is recommended for the transonic flow with shock waves. In the current work since there is no shock in the flow, the $\epsilon = 0.3$ is used.

The viscous terms are discretized by a fully conservative fourth-order accurate finite central differencing scheme suggested by Shen et al. [16, 17].

2.6 Boundary Conditions

Steady state freestream conditions including total pressure, total temperature, and two flow angles are specified for the upstream portion of the far field boundary. For far field downstream boundary, the static pressure is specified as freestream value to match the intended freestream Mach number. The streamwise gradients of other variables are forced to vanish. The periodic boundary condition is used in spanwise direction. The wall treatment suggested in [15] to achieve flux conservation by shifting half interval of the mesh on the wall is employed. If the wall surface normal direction is in η-direction, the no slip condition is enforced on the surface by computing the wall inviscid flux $F_{1/2}$ in the following manner:

$$\mathbf{F_w} = \begin{pmatrix} \rho V \\ \rho u V + p\eta_x \\ \rho v V + p\eta_y \\ \rho w V + p\eta_z \\ (\rho e + p)V \end{pmatrix}_w = \begin{pmatrix} 0 \\ p\eta_x \\ p\eta_y \\ p\eta_z \\ 0 \end{pmatrix}_w \tag{63}$$

Table 1: Computational parameters for the flat plate validation

cases	Mach	Reynolds	Mesh $N_\xi \times N_\eta \times N_\zeta$	Δx^*	Δy_1	Δz	Δx^+	Δy_1^+	Δz^+
1	0.1	1,000,000	$120 \times 120 \times 5$	0.0084	1.0e-5	0.0022	336	0.40	88
2	0.1	2,000,000	$120 \times 120 \times 5$	0.0084	1.0e-6	0.0022	672	0.08	176
3	0.1	6,500,000	$120 \times 120 \times 5$	0.0084	1.0e-6	0.0022	1764	0.21	462
4	0.1	10,000,000	$120 \times 120 \times 5$	0.0084	1.0e-6	0.0022	3024	0.36	792
5	0.1	20,000,000	$120 \times 120 \times 5$	0.0084	1.0e-6	0.0022	7392	0.88	1936
6	0.1	1,000,000	$300 \times 120 \times 5$	0.00133	1.0e-5	0.0022	53.3	0.40	88
7	0.1	2,000,000	$300 \times 120 \times 5$	0.00133	1.0e-6	0.0022	106.4	0.08	176
8	0.1	6,500,000	$300 \times 120 \times 5$	0.00133	1.0e-6	0.0022	279.3	0.21	462
9	0.1	10,000,000	$300 \times 120 \times 5$	0.00133	1.0e-6	0.0022	478.8	0.36	792
10	0.1	20,000,000	$300 \times 120 \times 5$	0.00133	1.0e-6	0.0022	1170.4	0.88	1936
11	0.6	1,000,000	$120 \times 120 \times 5$	0.0084	1.0e-5	0.0022	336	0.40	88
12	0.6	2,000,000	$120 \times 120 \times 5$	0.0084	1.0e-6	0.0022	672	0.08	176
13	0.6	6,500,000	$120 \times 120 \times 5$	0.0084	1.0e-6	0.0022	1764	0.21	462
14	0.6	10,000,000	$120 \times 120 \times 5$	0.0084	1.0e-6	0.0022	3024	0.36	792
15	0.6	20,000,000	$120 \times 120 \times 5$	0.0084	1.0e-6	0.0022	7392	0.88	1936
16	0.6	1,000,000	$300 \times 120 \times 5$	0.00133	1.0e-5	0.0022	53.3	0.40	88
17	0.6	2,000,000	$300 \times 120 \times 5$	0.00133	1.0e-6	0.0022	106.4	0.08	176
18	0.6	6,500,000	$300 \times 120 \times 5$	0.00133	1.0e-6	0.0022	279.3	0.21	462
19	0.6	10,000,000	$300 \times 120 \times 5$	0.00133	1.0e-6	0.0022	478.8	0.36	792
20	0.6	20,000,000	$300 \times 120 \times 5$	0.00133	1.0e-6	0.0022	1170.4	0.88	1936

*all the grid distance information refers to the local grid size denoted in Fig. 1.

3 Results and Discussion

3.1 IDDES Validation of the 3D Flat Plate Boundary Layer

To test the IDDES implementation, simulation of the 3D flat plate turbulent boundary layer flow is conducted to validate with the law of the wall. The simulations are conducted at different Mach numbers, Reynolds numbers and mesh sizes. To study the sensitivity of turbulence models on compressibility, two Mach number of 0.1 and 0.6 are used in the simulation. Four different Reynolds number in the range of 1,000,000 to 20,000,000 are simulated. Since mesh sizes have significant impact on the DES-family models, different meshes are constructed for comparison. As shown in Fig. 1, two computational meshes are constructed with size of $120 \times 120 \times 5$ and $300 \times 120 \times 5$ in streamwise, normal to the wall and spanwise direction. The computational meshes are constructed to test the ambiguous grid spacing, as indicated by Spalart[3]. The coarse mesh is constructed to have streamwise grid spacing, $\Delta_{\parallel}$ (or Δx for the present 3D flat plate) about 0.63-0.75 of the turbulent boundary layer thickness, calculated by $\delta = 0.37(Re_L)^{-0.2}L$. The fine mesh is constructed to have streamwise grid spacing, $\Delta_{\parallel}$ (or Δx and Δz for the present 3D flat plate) about 0.09-0.118 of the turbulent boundary layer thickness. The first grid dimensionless distance normal to the wall has the $y^+(=\frac{u_\tau y}{\nu})$ is less than unity. Periodic boundary conditions are applied in the spanwise directions. No-slip wall boundary conditions are implemented on the flat plate surface. The 3D flat plate boundary layer test cases are summarized in table 1.

Fig. 3, 4, 5, 6 and 7 present the turbulent boundary layer profiles computed by the S-A URANS model, and DES family models(DES97, DDES and IDDES) at different Reynolds numbers with coarse and fine meshes. In order to demonstrate the IDDES improvement on the MSD and LLM problems over the DES97 and DDES, the meshes are specifically generated in the ambiguous grid size range. The boundary layer size and mesh size in the test region are illustrated as in Fig. 2

The first cases has the Reynolds number of 1,000,000 and the results are shown in Fig. 3. For the coarse mesh simulation at both Mach number of 0.1 and 0.6, all the simulated boundary layer profiles are in good agreement with the law of the wall. However, for the fine mesh simulation, the profiles calculated by DES97 and DDES are significantly deviated away from the velocity log profile for both two Mach numbers. This phenomena is referred as the Log Layer Mismatch(LLM) [3], [5],[18]. The higher u_+ obtained by the DES97 and DDES calculation indicates that the wall shear stress τ_w is underpredicted. Similar trends are observed in the Reynolds numbers of 2,000,000 and 6,500,000.

At the Reynolds numbers of 10,000,000, the accuracy of DES97 and DDES has a significant difference for the fine mesh at the Mach number of 0.1. This phenomena is refereed as the Model Stress Depletion(MSD) by Spalart[3]. However, at the high Mach number of 0.6, the predicted velocity profiles show little difference between the DES97 and DDES. For the coarse mesh, both the velocity profiles predicted by DES97 and DDES agree well with the law of the wall.

At the highest Reynolds number of 20,000,000, the results are quite different for DES97 and DDES with the variation of Mach number. At Mach number of 0.1, DES97 and DDES obtain the velocity profiles that are deviated from the law of the wall in at the coarse mesh and fine mesh. At the high Mach number of 0.6, all the simulations agree well with the law of the wall. As always, the IDDES outperforms all the DES family models with excellent prediction for all the cases.

In Fig. 8, the simulated velocity profile ratio ($\frac{u}{U_\infty}$), the dimensionless turbulent eddy viscosity($0.002\frac{\nu_t}{\nu}$), blending function f_d, and elevating function f_e are all predicted well by IDDES. The turbulent eddy viscosity predicted by the IDDES is fully preserved inside the turbulent boundary layer. The turbulent eddy viscosity ν_t reaches the maximum value at the outer layer of boundary layer and decays rapidly when it approaches the wall and the edge of the boundary layer. The blending function f_d behaves as the expected transition in the buffer layer from near wall RANS scale to LES scale near the boundary layer edge. The elevating function reaches the maximum at $y/\delta = 0.3$.

3.2 IDDES Investigation of the NACA0012 Airfoil Stalled Flows

Table 2: Simulation cases setup for NACA0012

Case	AoA	Grid size	Δx^*	Δy_1	Δz	Δx^+	Δy_1^+	Δz^+
1	5	$192 \times 100 \times 30$	0.00020-0.02681	1e-5	0.0344	10-1340	0-1	1720
2	5	$288 \times 100 \times 30$	0.00013-0.01788	1e-5	0.0344	6.6-894	0-1	1720
3	17	$192 \times 100 \times 30$	0.00020-0.02681	1e-5	0.0344	10-1340	0-1	1720
4	17	$288 \times 100 \times 30$	0.00013-0.01788	1e-5	0.0344	6.6-894	0-1	1720
5	45	$192 \times 100 \times 30$	0.00020-0.02681	1e-5	0.0344	10-1340	0-1	1720
6	45	$288 \times 100 \times 30$	0.00013-0.01788	1e-5	0.0344	6.6-894	0-1	1720
7	60	$192 \times 100 \times 30$	0.00020-0.02681	1e-5	0.0344	10-1340	0-1	1720
8	60	$288 \times 100 \times 30$	0.00013 -0.01788	1e-5	0.0344	6.6-894	0-1	1720

Simulation of the NACA0012 airfoil stalled flows at four different angle of attack of $5°, 17°, 45°, 60°$ is carried out to investigate the capability of the IDDES for predicting flows with different large turbulent structures, including: a flow with minor separation near the trailing edge(AoA=5°), stall flow with large wake separations(AoA=17°) and stall flows with massive flow separation(AoA=45°, 60°).

For vortical flows, computational results of Q-criterion are used to represent vortices. The Q-criterion define vortices as areas where the vorticity magnitude is greater than the magnitude of rate-of-strain[22]. Q=0 represents that the local balance between shear strain rate and vorticity magnitude. $Q = \frac{1}{2}(\|\overline{\Omega}\|^2 - \|\overline{S}\|^2)$ where, $\overline{S}$ is the rate-of-strain tensor, and $\overline{\Omega}$ is the vorticity tensor

The Reynolds number based on the airfoil chord (c) is 1.3×10^6 and Mach number based on the freestream velocity (U_∞) is 0.5. The experimental lift and drag coefficients at $R_e = 2 \times 10^6$[19, 20, 21] are used for comparison, which is acceptable since the Reynolds number dependence is weak after stall at high Reynolds number greater than 1×10^5[9, 19, 20]. Unsteady simulations are performed over 200-250 dimensionless time ($T = c/U_\infty$) with the implicit pseudo time step iterations. The CFL number in current simulation is 1.0-5.0. The number of pseudo time steps within each physical time step is determined by having the residual reduced by at least three orders of magnitude, which is usually achieved within 20 iterations. The dimensionless physical time step of $0.02c/U_\infty$ is used.

Fig. 9 shows the 3D NACA0012 computational coarse and fine meshes topology. The coarse and fine computational meshes are constructed using an O-mesh topology with mesh size of $192 \times 100 \times 30$ and $288 \times 100 \times 30$ in streamwise, normal to the wall and spanwise direction. The first grid spacing on airfoil surface yields y^+ less than unity. Calculated first wall normal mesh distance is shown in Fig.10. All the mesh parameters are summaried in table 2. The far field boundary is set about 80 times of the airfoil chord length. The span length used is the same as the chord. Periodic boundary conditions are employed in the spanwise direction. No-slip wall boundary conditions are enforced on the airfoil surface.

As shown in Fig. 11, the time-averaged lift and drag coefficient (C_l, C_d) at different AoAs are compared with the experimental data[9, 20]. At the AoA of 5°, all the S-A URANS, DDES and IDDES calculated lift and drag coefficients agree well with the experiment. At the AoA of 17°, the S-A URANS predicted lift and drag coefficient agrees well with the experiment, whereas the DDES and IDDES predicted lift coefficients have small deviations. The URANS computation over-predicts the lift and drag coefficient at AoA=45° and 60° by about 30%, whereas the DDES and IDDES accurately predict the lift and drag at these high AoA with massive flow separations.

Fig. 12 gives the lift and drag coefficient history at AoA=5°. Constant lift and drag coefficients are achieved from all unsteady CFD calculations. Time-averaged Mach number contours are presented in Fig. 13. Thicker boundary layer the trailing edge is observed. The instantaneous pressure and viscous drag coefficient components Cd_p and Cd_v are given in Fig. 14. The pressure and viscous forces are in the same order of magnitude. Both of them have significant contribution to the resultant drag force.

Fig. 15 presents the instantaneous lift and drag coefficient at AoA=17°. IDDES and DDES obtain the lift and drag coefficient oscillating with time due to vortex shedding, whereas constant lift and drag coefficients are obtained by the URANS computation. This difference indicates that flow separation is phase-locked by the URANS model, which is inappropriate for real flow with large separations. From the Cl-AoA curve(see 11), the airfoil flow approaches dynamic stall region at near AoA=17° where the lift and drag coefficients have a dramatic drop. Fig. 16 presents the time-averaged Mach number contours at AoA=17°. The URANS simulated Mach number contours show little difference for coarse and fine mesh. Comparing the fine mesh and coarse mesh simulation, DDES and IDDES predict large wake size than with the fine mesh. Fig. 17 presents the 3D iso-surfaces of Q-criterion=0 for S-A URANS, DDES and IDDES computations using the fine mesh. The URANS simulates the vortical structures as two dimensional large organized harmonic vortex shedding. The vortical flow structures calculated by IDDES are three dimensional and chaotic with the streamwise, spanwise and transverse vortices.

Fig. 18 presents the lift and drag coefficients history at AoA of 45°. The URANS simulation obtains the harmonically oscillating lift and drag coefficients, whereas the lift and drag coefficients calculated by the DDES and IDDES oscillates without standard harmonics. The time-averaged Mach number contours are given in Fig. 19. Fig. 20 presents the 3D iso-surfaces of Q-criterion=0 for S-A URANS, DDES and IDDES computations using the fine mesh. Again, the URANS predicts large scale structured vortex shedding, whereas the DDES and IDDES achieve high chaotic large and small scale vortices. Both DDES and IDDES capture the massively separated flow with 3D streamwise, transverse, and spanwise vortical structures, while URANS obtains the vortex shedding that are dominant with spanwise vorticity. Such predicted vortical structures difference is believed to make the quantitative drag accuracy as reflected in Fig. 11.

Fig. 21 presents the instantaneous Mach contours at three different span cross-sections predicted by URANS. Flow structures are organized vortex shedding at different span cross-sections. Fig. 22 presents the instantaneous Mach contours at different span cross-section predicted by IDDES. Vortical flow structure and spanwise flow structures are very different from those of the URANS and are more chaotic and disorganized. Fig. 23 shows the instantaneous vorticity of 10% span, 50% span and 90% span predicted by IDDES simulation. The present S-A URANS results capture the phase locked vortex shedding phenomena that usually occurs at low Reynolds number flows, whereas IDDES shows more realistic and turbulent vortical flow structures in the regions of massive separations.

Fig. 24 gives the lift and drag coefficients history at AoA of 60°. Similar trends are observed with periodic lift and drag coefficients variation using the URANS and irregularly oscillating lift and drag coefficients using the DDES and IDDES. The time-averaged Mach number contours are given in Fig. 25. The IDDES and DDES predict larger separation regions than the S-A URANS model. The 3D iso-surfaces of Q-criterion=0 for S-A URANS, DDES and IDDES are given in Fig. 26. Similar to the previous massive separation case, the large scale phase-locked vortex shedding is achieved using S-A URANS and three dimensional small scale vortices are captured using DDES and IDDES. The capacity to capture more realistic flow structures by DDES and IDDES, which determines the accuracy of drag prediction for massive separated flows.

4 Conclusions

Comparative study of the S-A URANS, DDES and IDDES computation of the flat plate boundary layer and the stalled flow of the NACA0012 airfoil at different AoAs of 5°, 17°, 45°, and 60° . High order schemes are employed in current study with the fifth order WENO reconstruction for the inviscid fluxes and 4th order central differencing for the viscous fluxes. Simulation of turbulent boundary layer indicates that the IDDES predicts the law of the wall accurately for different mesh sizes, Reynolds numbers, and Mach numbers, whereas the DES97 and DDES obtain the velocity profile in the boundary layer with model stress depletion and log layer mismatched at certain conditions. For the NACA0012 stalled flows, at low and medium AOAs(=5°, 17°), the URANS, DDES, and IDDES all predict the drag accurately. However, for the massive separated flows at high AoAs(=45°, 60°), the URANS over-predicts the drag coefficient significantly by about 30%, whereas the DDES and IDDES predict the drag coefficient accurately. The vortical flow structures obtained by the URANS are highly-regularized vortex shedding dominated by the spanwise vorticity. The IDDES can resolve more realistic flow structures, including smaller scale vortices that are chaotic and disorganized with streamwise, transverse and spanwise vortices.

5 Acknowledgment

The computations are conducted on Pegasus super computer from Center of Computer Science at the University of Miami.

References

[1] J. A. Ekaterinaris and M. F. Platzer, "Computational prediction of airfoil dynamic stall," *Progress in aerospace sciences*, vol. 33, no. 11, pp. 759–846, 1998.

[2] Spalart, P.R., Jou, W.H., Strelets, M., and Allmaras, S.R., "Comments on the Feasibility of LES for Wings, and on a Hybrid RANS/LES Approach." Advances in DNS/LES, 1st AFOSR Int. Conf. on DNS/LES, Greyden Press, Columbus, H., Aug. 4-8, 1997.

[3] Spalart, P.R., Deck, S., Shur, M., and Squires, K.D., "A New Version of Detached-Eddy Simulation, Resistant to Ambiguous Grid Densities," *Theoritical and Computational Fluid Dynamics*, vol. 20, pp. 181–195, DOI: 10.1007/s00162–006–0015–0, 2006.

[4] A. K. Travin, M. L. Shur, P. R. Spalart, and M. K. Strelets, "Improvement of delayed detached-eddy simulation for les with wall modelling," in *ECCOMAS CFD 2006: Proceedings of the European Conference on Computational Fluid Dynamics, Egmond aan Zee, The Netherlands, September 5-8, 2006*, Delft University of Technology; European Community on Computational Methods in Applied Sciences (ECCOMAS), 2006.

[5] M. L. Shur, P. R. Spalart, M. K. Strelets, and A. K. Travin, "A hybrid rans-les approach with delayed-des and wall-modelled les capabilities," *International Journal of Heat and Fluid Flow*, vol. 29, no. 6, pp. 1638–1649, 2008.

[6] C. Mockett, *A Comprehensive Study of Detached Eddy Simulation.* Univerlagtuberlin, 2009.

[7] Morton, S.A., Forsythe, J.R., Squires, K.D., Cummings, R.M., "Detached-Eddy Simulations of Full Aircraft Experincing Massively Separated Flows." The 5th Asian Computational Fluid Dynamics Conference, Busan, Korea, October 27 - 30, 2003.

[8] N. Durrani and N. Qin, "Behavior of detached-eddy simulations for mild airfoil trailing-edge separation," *Journal of Aircraft*, vol. 48, no. 1, pp. 193–202, 2011.

[9] H.-S. Im and G.-C. Zha, "Delayed detached eddy simulation of airfoil stall flows using high-order schemes," *Journal of Fluids Engineering*, vol. 136, no. 11, p. 111104, 2014.

[10] P. R. Spalart and S. R. Allmaras, "A one-equation turbulence model for aerodynamic flows," in *30th Aerospace Sciences Meeting and Exhibit, Aerospace Sciences Meetings, Reno, NV, USA, AIAA Paper 92-0439*, 1992.

[11] Jameson, A., "Time Dependent Calculations Using Multigrid with Applications to Unsteady Flows Past Airfoils and Wings." AIAA Paper 91-1596, 1991.

[12] Zha, G.C., Shen, Y.Q. and Wang, B.Y., "An improved low diffusion E-CUSP upwind scheme ," *Journal of Computer and Fluids*, vol. 48, pp. 214–220, Sep. 2011.

[13] Edwards, J.R., "A Low-Diffusion Flux-Splitting Scheme for Navier-Stokes Calculations," *Computer & Fluids*, vol. 6, pp. 635–659,doi:10.1016/S0045–7930(97)00014–5, 1997.

[14] Shen, Y.Q., and Zha, G.C., "Improvement of the WENO Scheme Smoothness Estimator," *International Journal for Numerical Methods in Fluids*, vol. 64,, pp. 653–675, DOI:10.1002/fld.2186, 2009.

[15] Shen, Y.Q., Zha, G.C., and Wang, B.Y., "Improvement of Stability and Accuracy of Implicit WENO Scheme," *AIAA Journal*, vol. 47, pp. 331–334, DOI:10.2514/1.37697, 2009.

[16] Shen, Y.Q., and Zha, G.C., "Large Eddy Simulation Using a New Set of Sixth Order Schemes for Compressible Viscous Terms," *Journal of Computational Physics*, vol. 229, pp. 8296–8312, doi:10.1016/j.jcp.2010.07.017, 2010.

[17] Shen, Y.Q., Zha, G.C., and Chen, X., "High Order Conservative Differencing for Viscous Terms and the Application to Vortex-Induced Vibration Flows," *Journal of Computational Physics*, vol. 228(2), pp. 8283–8300, doi:10.1016/j.jcp.2009.08.004, 2009.

[18] N. Nikitin, F. Nicoud, B. Wasistho, K. Squires, and P. Spalart, "An approach to wall modeling in large-eddy simulations," *Physics of Fluids (1994-present)*, vol. 12, no. 7, pp. 1629–1632, 2000.

[19] Hoerner, S.F., "Fluid-Dynamic Drag." , 1965.

[20] Shur, M.L., Spalart, P.R., Strelets, M., and Travin, A., "Detached-Eddy Simulation of an Airfoil at High Angle of Attack", 4th Int. Symp. Eng. Turb. Modelling and Measurements, Corsica." May 24-26, 1999.

[21] Jogansen, J. and Sorensen, N., "Application of a Detached Eddy Simulation Model on Airfoil Flows." IEA 2000, 2000.

[22] V. Kolář, "Vortex identification: New requirements and limitations," *International journal of heat and fluid flow*, vol. 28, no. 4, pp. 638–652, 2007.

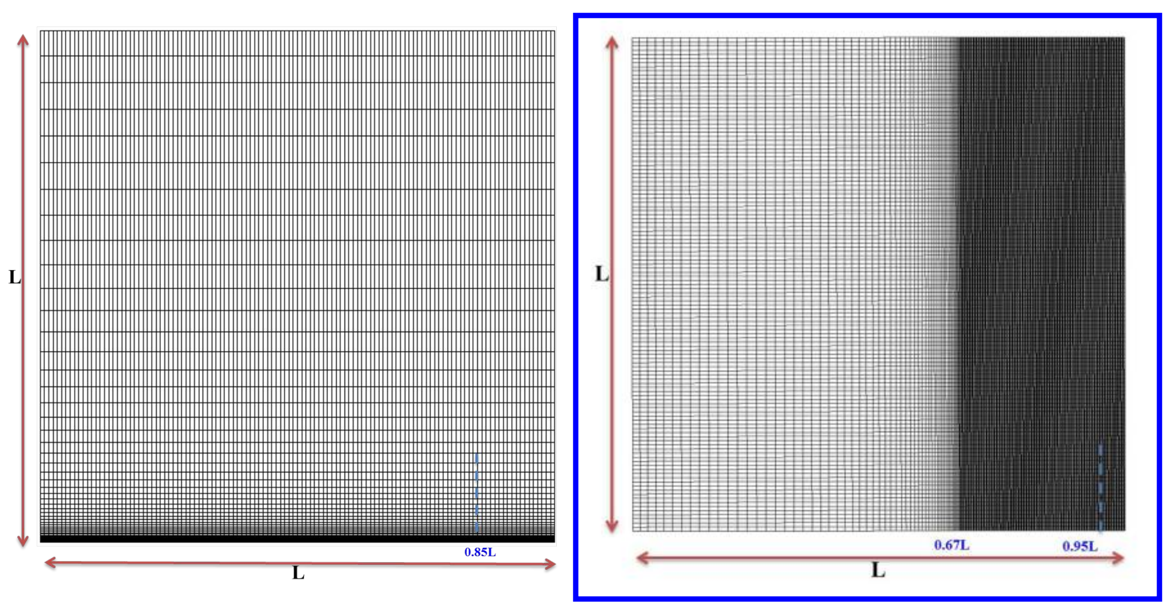

Figure 1: Computational coarse and fine mesh for flate plate

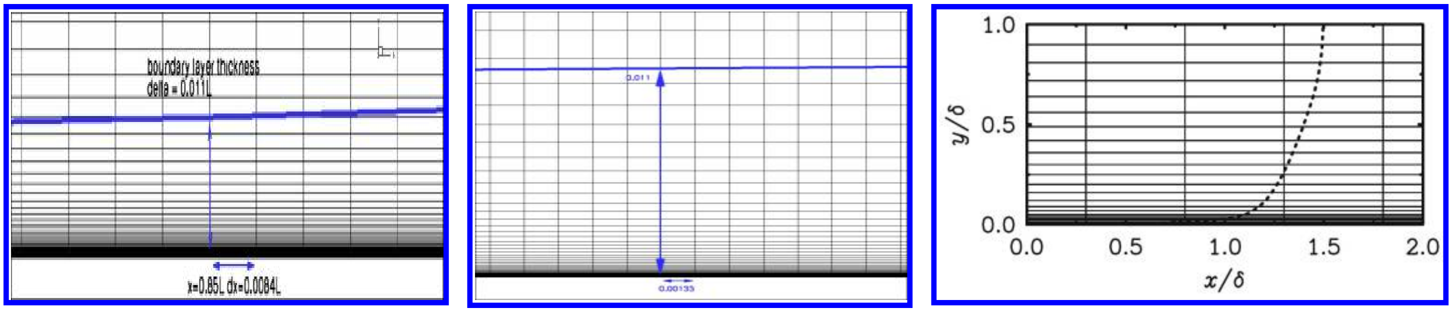

coarse mesh | fine mesh | ambigious grid spacing

Figure 2: Typical mesh size and boundary layer thickness in the test section for coarse and fine mesh, shown are simulations with Reynolds number of 20,000,000

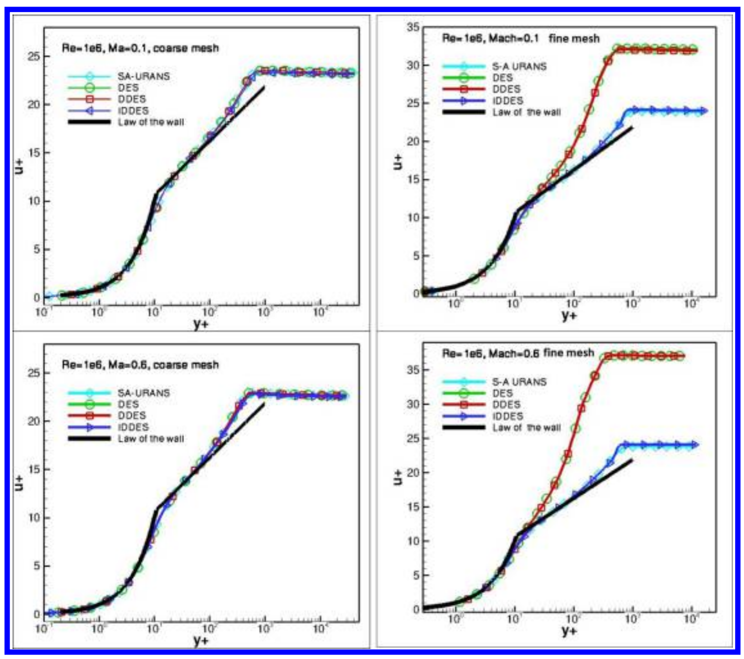

Figure 3: Mean velocity profiles calculated at Re=1000000, comparing to the law of the wall(Mach = 0.1(top figure), 0.6(bottom figure), coarse mesh(Left figure) and fine mesh(Right figure))

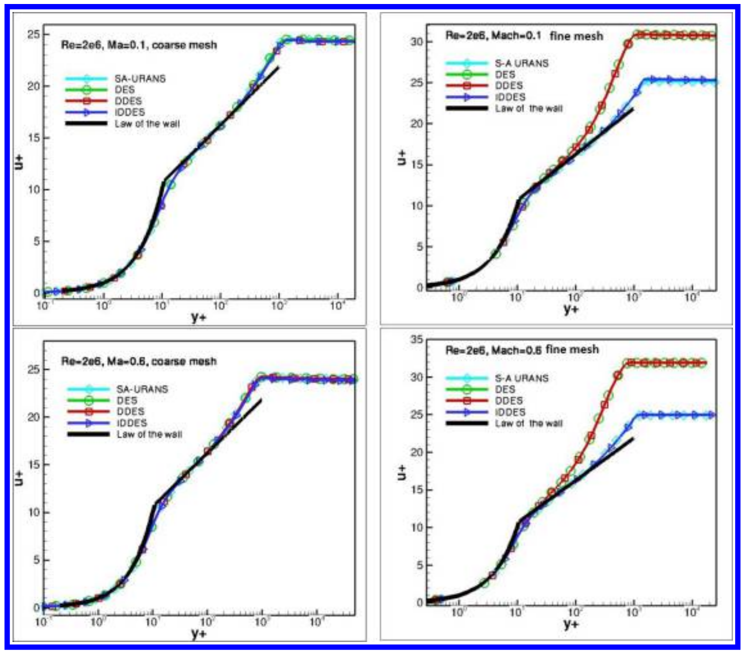

Figure 4: Mean velocity profiles calculated at Re=2000000, comparing to the law of the wall(Mach = 0.1(top figure), 0.6(bottom figure), coarse mesh(Left figure) and fine mesh(Right figure))

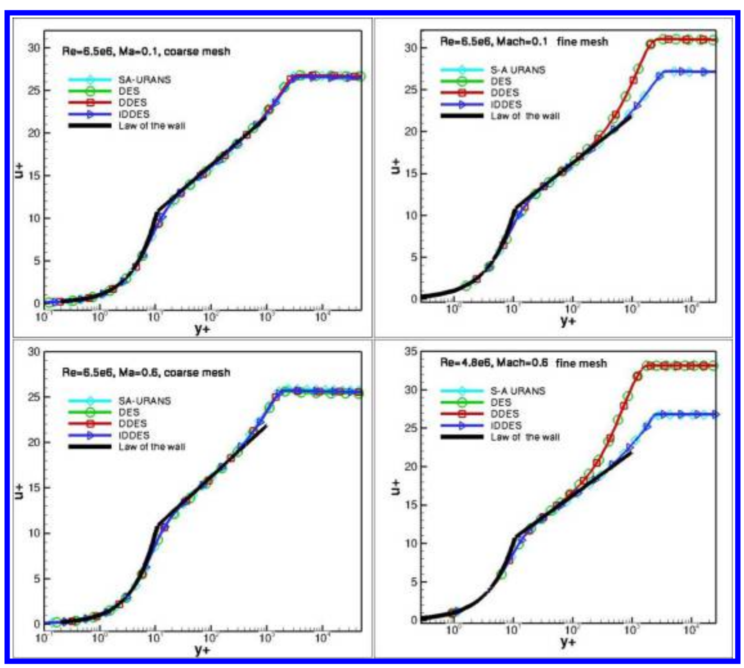

Figure 5: Mean velocity profiles calculated at Re=6500000, comparing to the law of the wall(Mach = 0.1(top figure), 0.6(bottom figure), coarse mesh(Left figure) and fine mesh(Right figure))

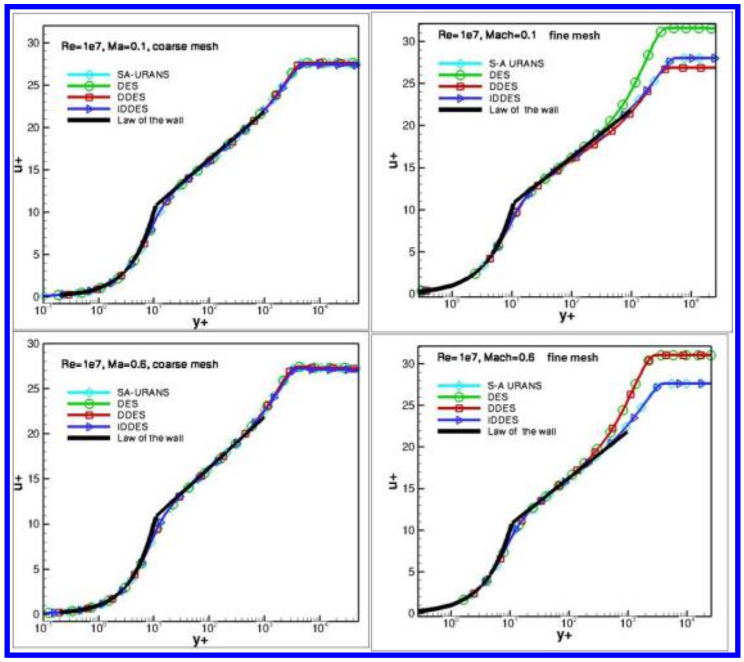

Figure 6: Mean velocity profiles calculated at Re=10000000, comparing to the law of the wall(Mach = 0.1(top figure), 0.6(bottom figure), coarse mesh(Left figure) and fine mesh(Right figure))

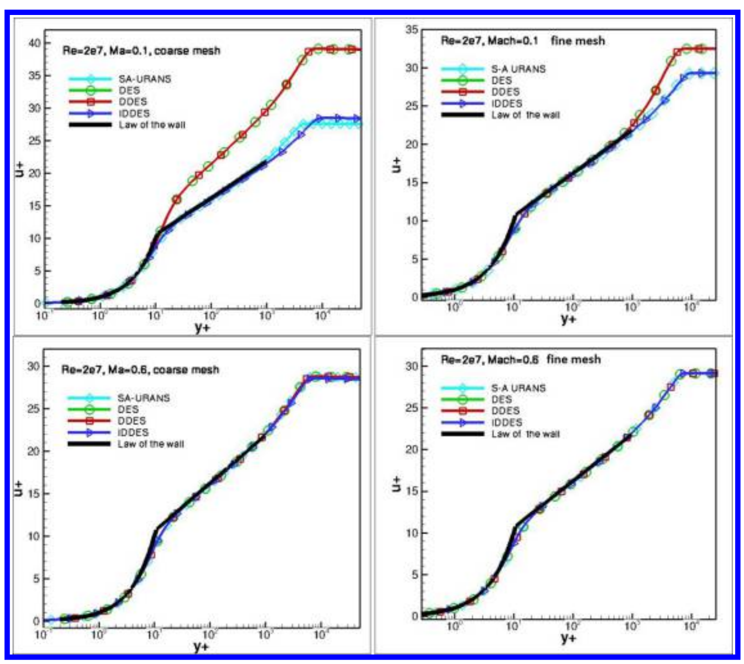

Figure 7: Mean velocity profiles calculated at Re=20000000, comparing to the law of the wall(Mach = 0.1(top figure), 0.6(bottom figure), coarse mesh(Left figure) and fine mesh(Right figure))

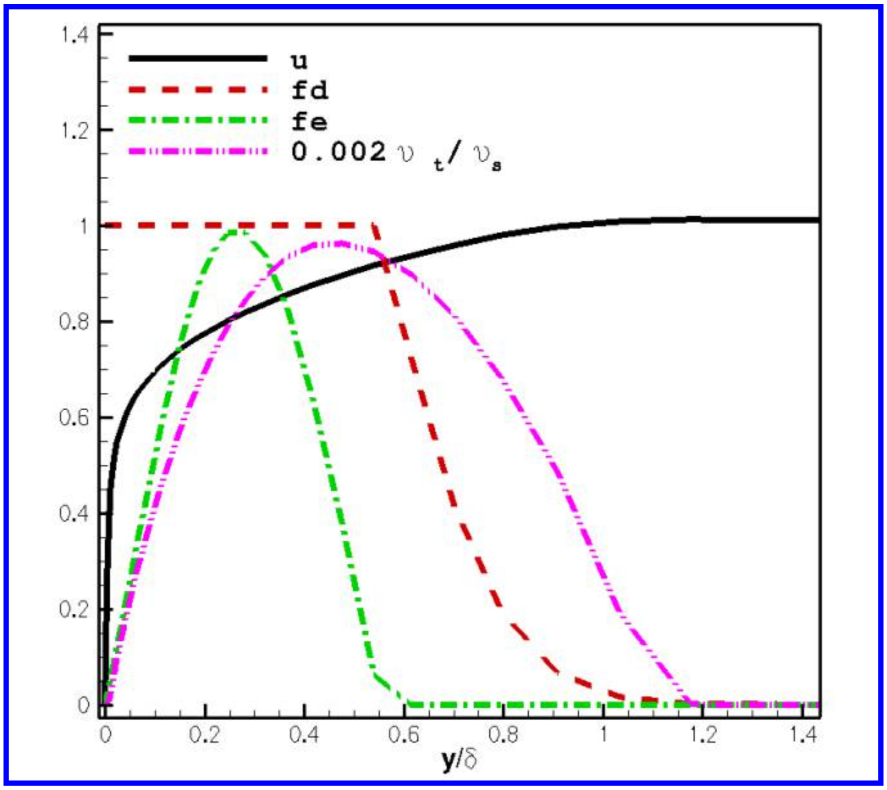

Figure 8: Distributions of $u/U_\infty, 0.002\frac{\nu_t}{\nu}, f_d, f_e$ in the flat plate boundary layer

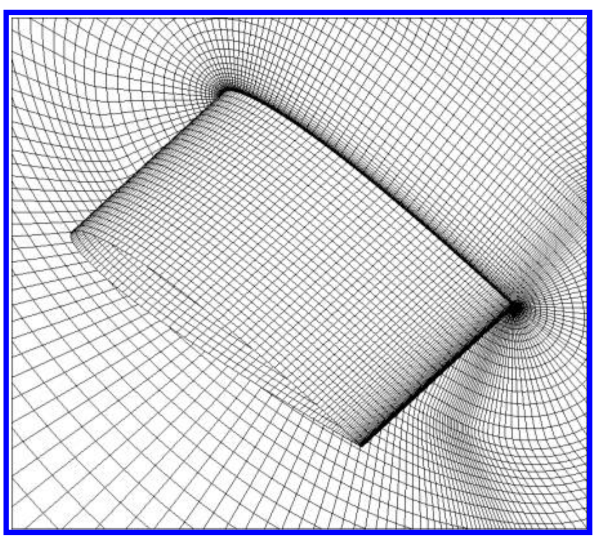

coarse mesh

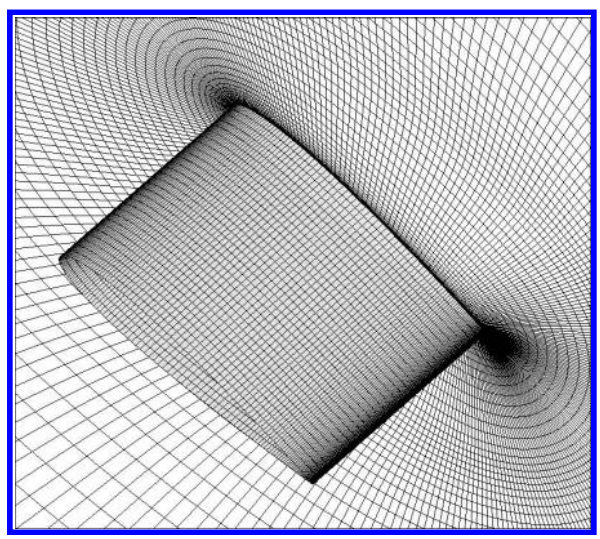

fine mesh

Figure 9: Computational meshes of NACA0012 computation

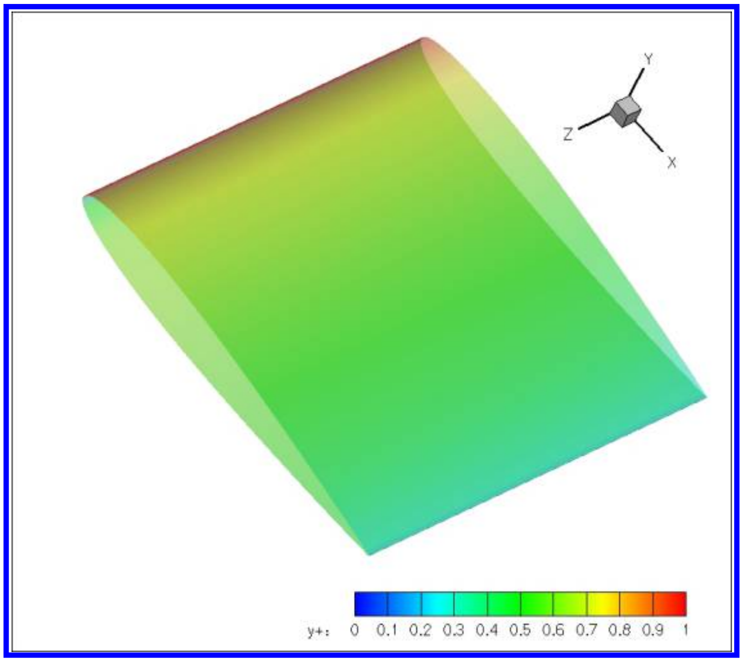

Figure 10: Calculated wall normal distance on the NACA 0012 airfoil surface.

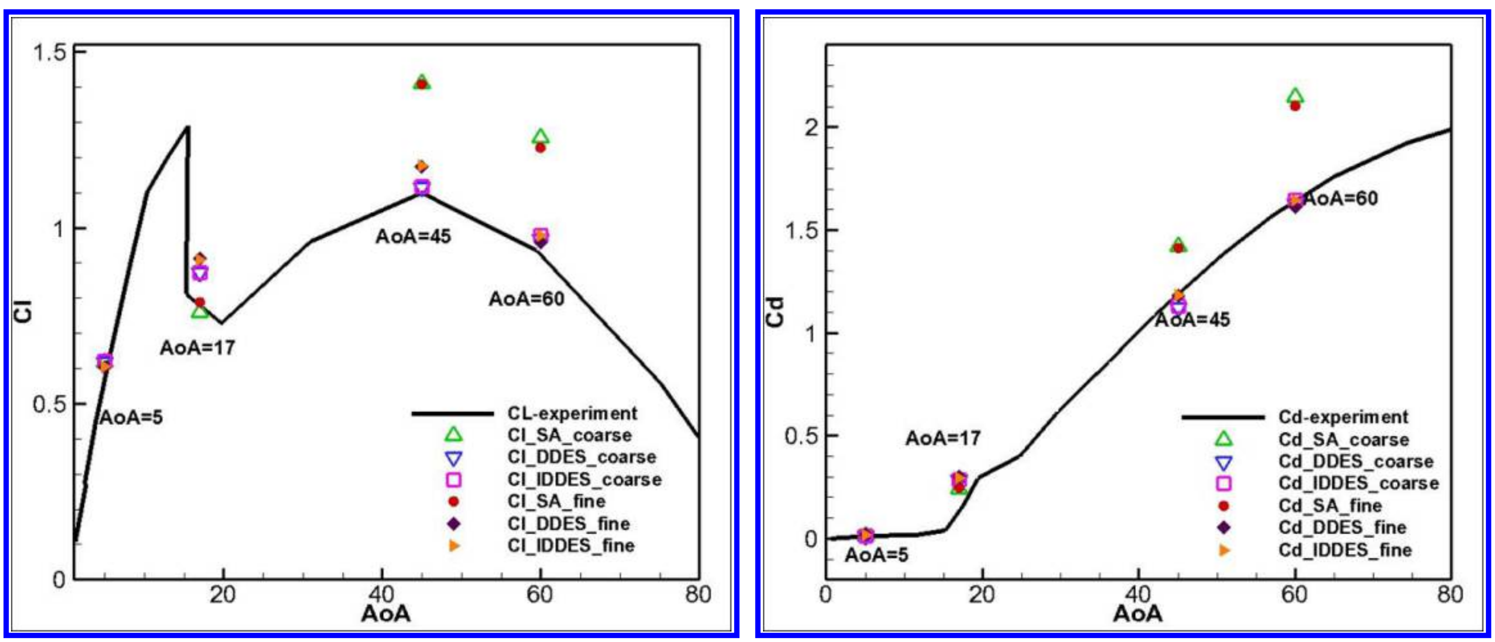

Figure 11: Time-averaged lift and drag coefficients of all NACA0012 computations and comparison with experimental data.

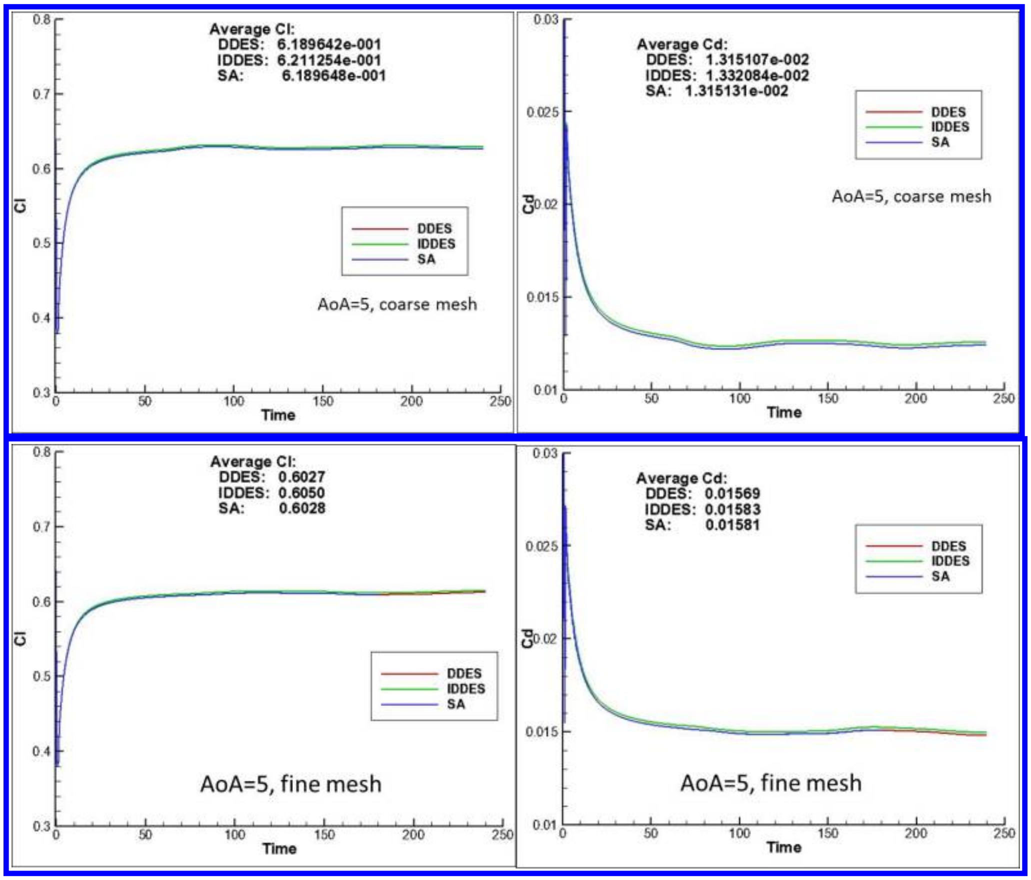

Figure 12: Lift and drag coefficient history at AoA = 5°.

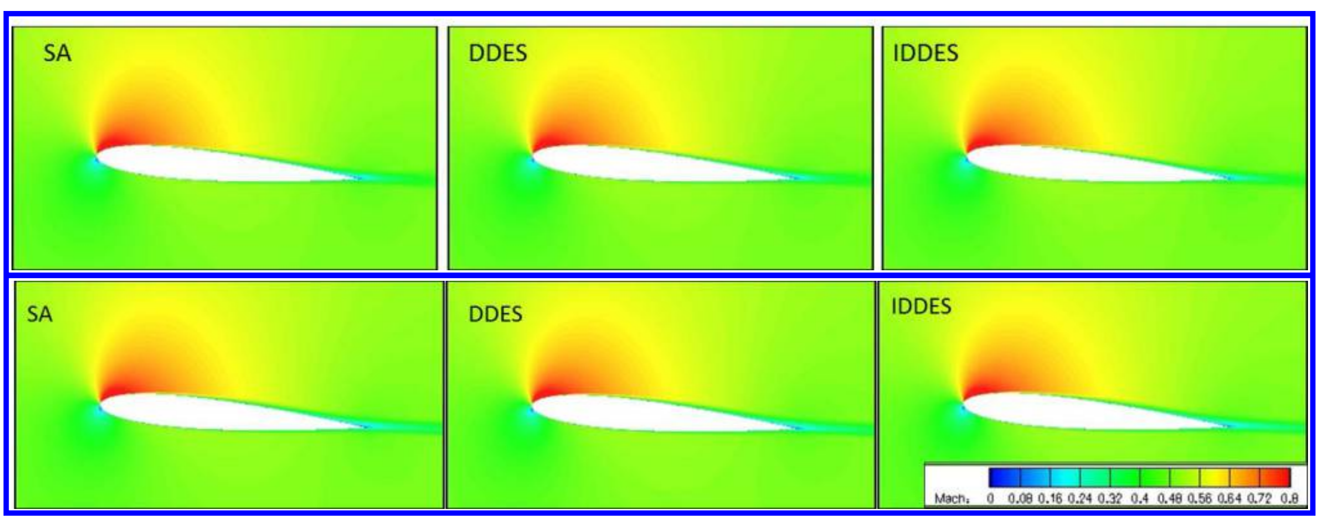

Figure 13: Time-averaged Mach contours at AoA = 5° in simulation with coarse(top) and fine(bottom) mesh.

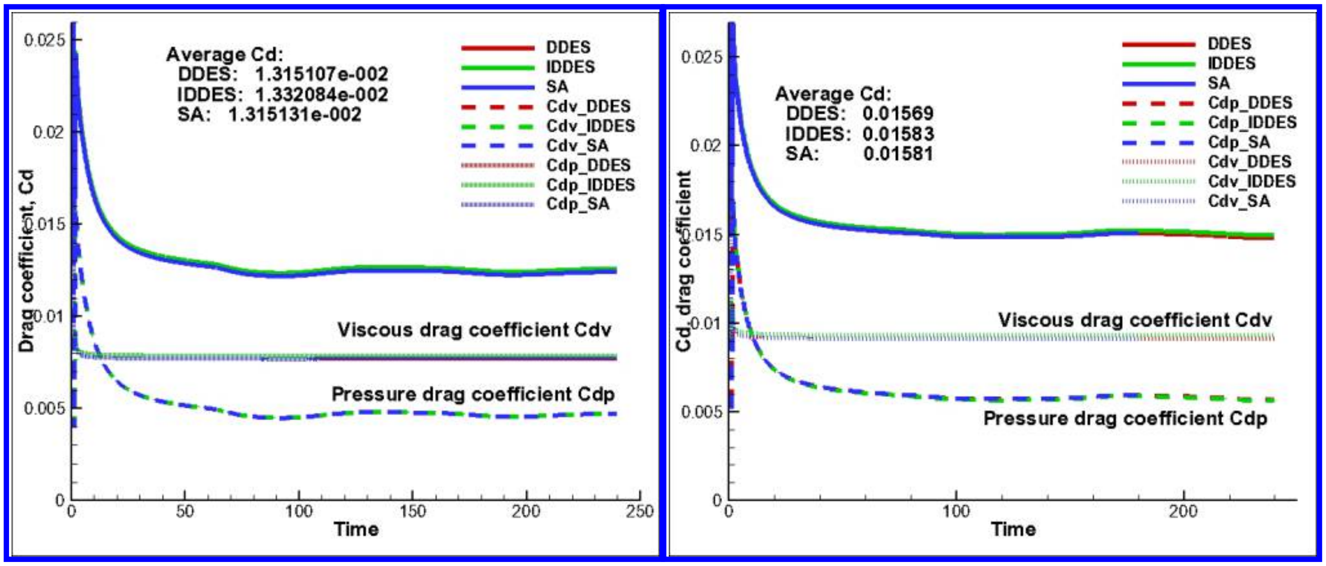

Figure 14: Viscous and pressure drag coefficient history at AoA = 5°.

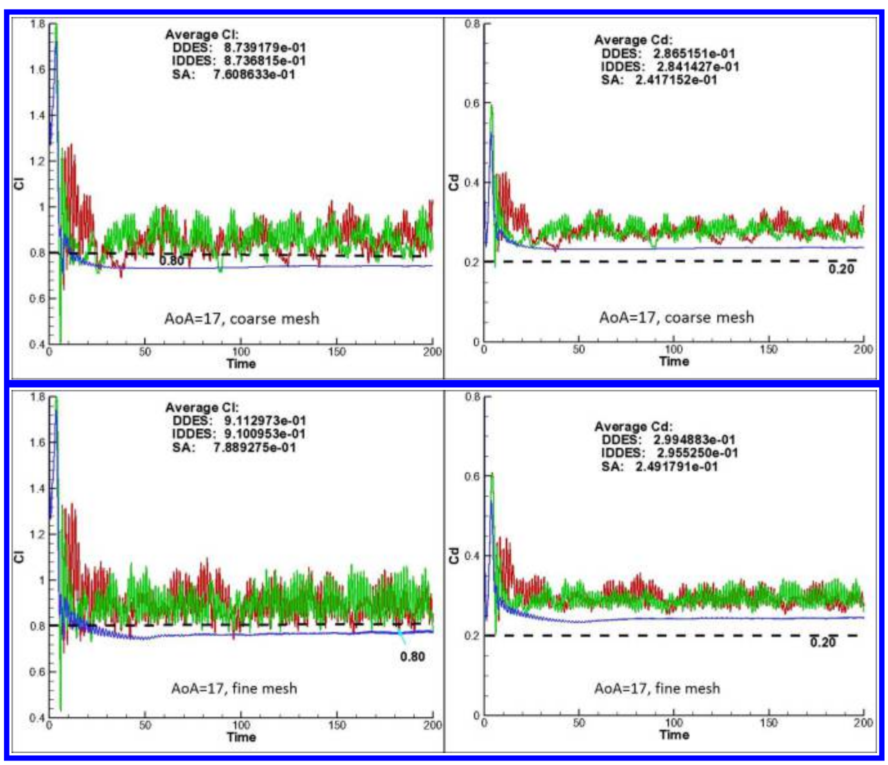

Figure 15: Lift and drag coefficient history at AoA = 17°.

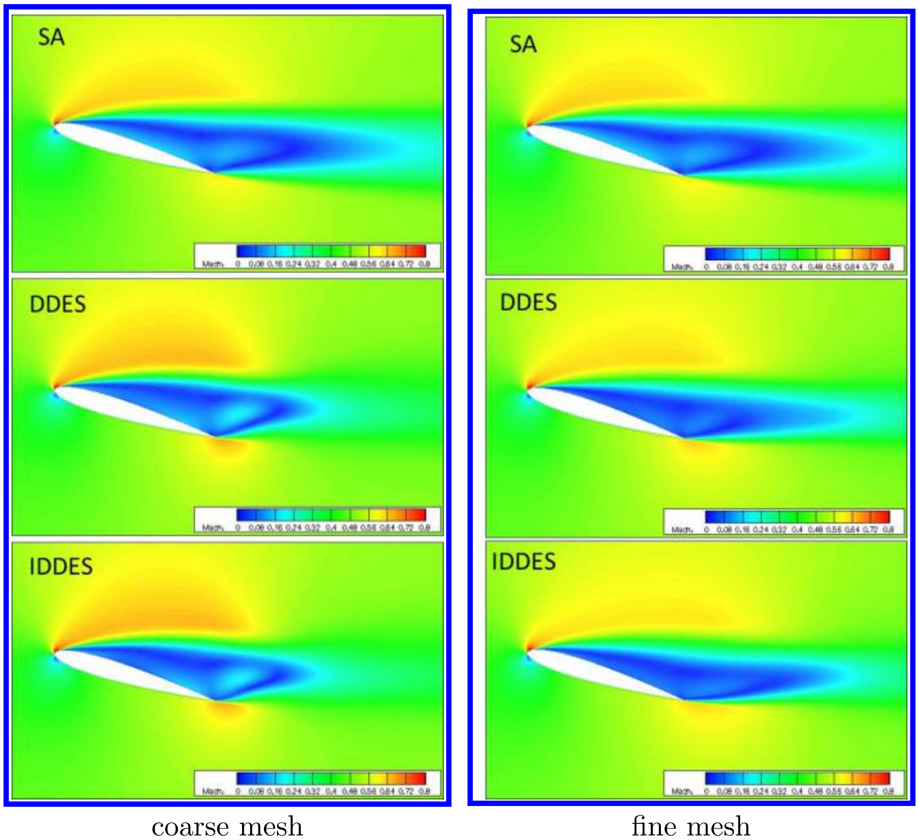

Figure 16: Time-averaged Mach contours at AoA = 17° in simulation with coarse(left) and fine(right) mesh.

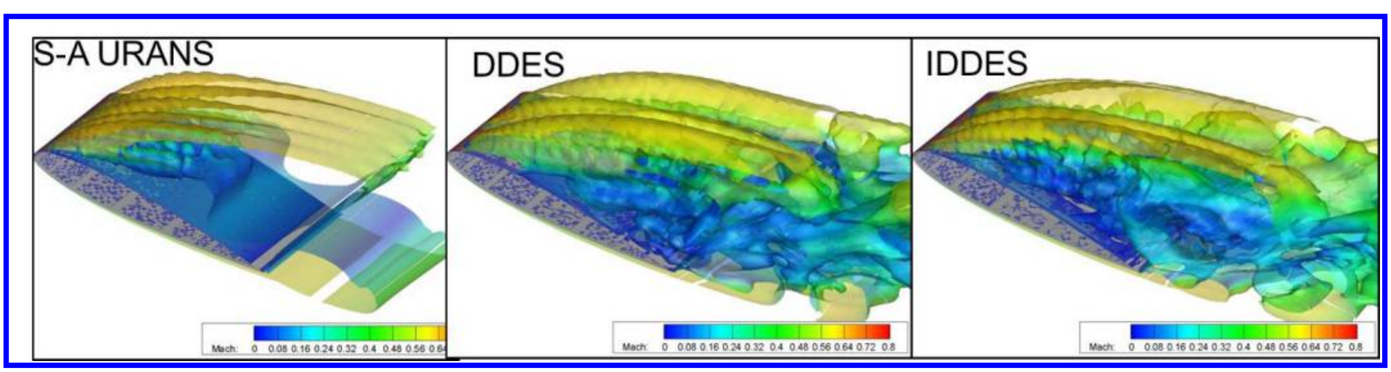

Figure 17: Iso-surfaces of the instantaneous Q-criterion=0, shown are the results of the S-A URANS, DDES and IDDES at AoA = 17°.

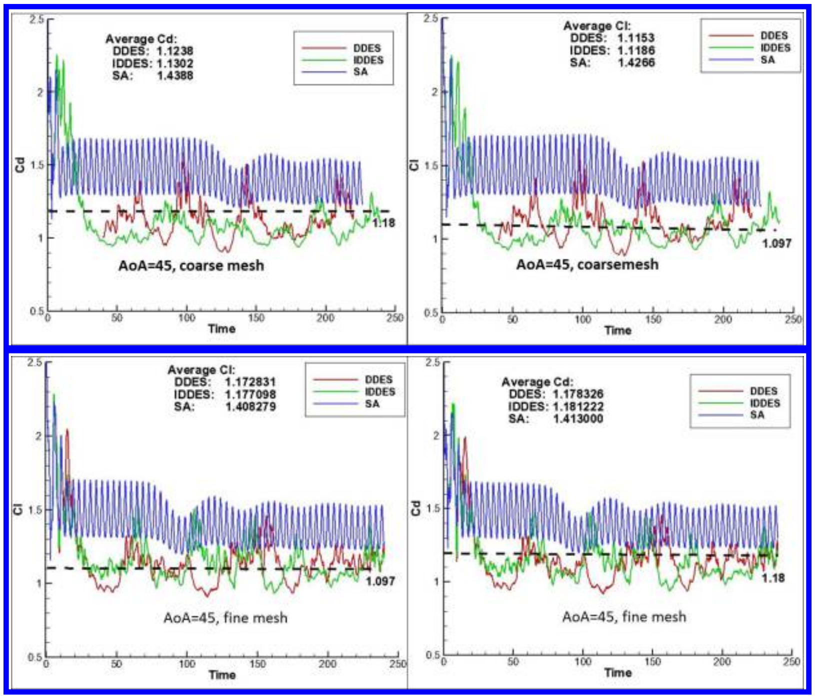

Figure 18: Lift and drag coefficient history at AoA = 45°.

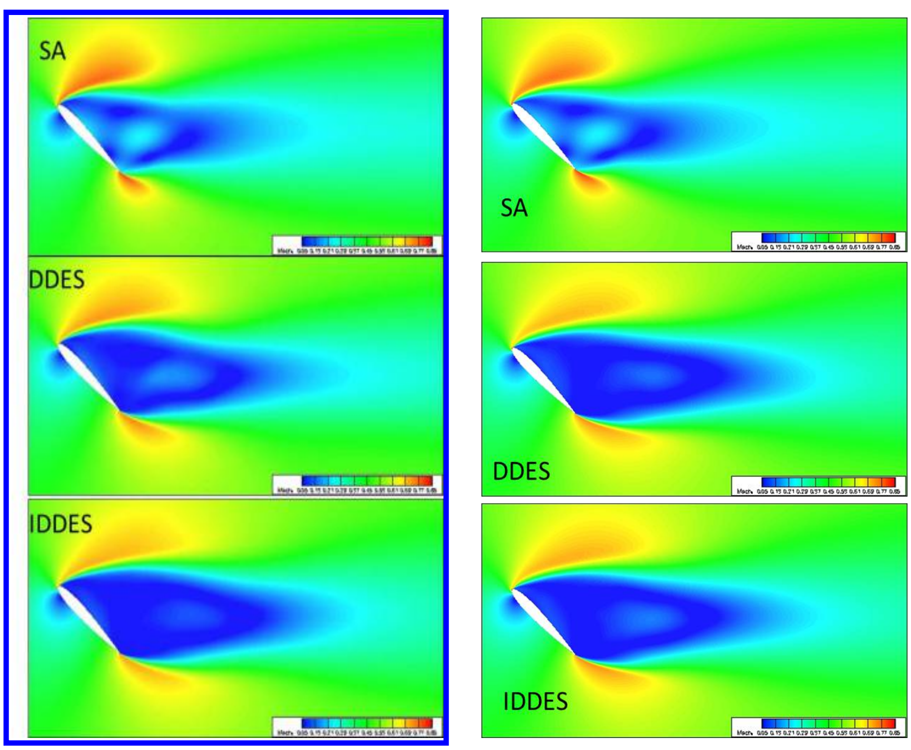

Figure 19: Time-averaged Mach contours at AoA = 45° in simulation with coarse(left) and fine(right) mesh.

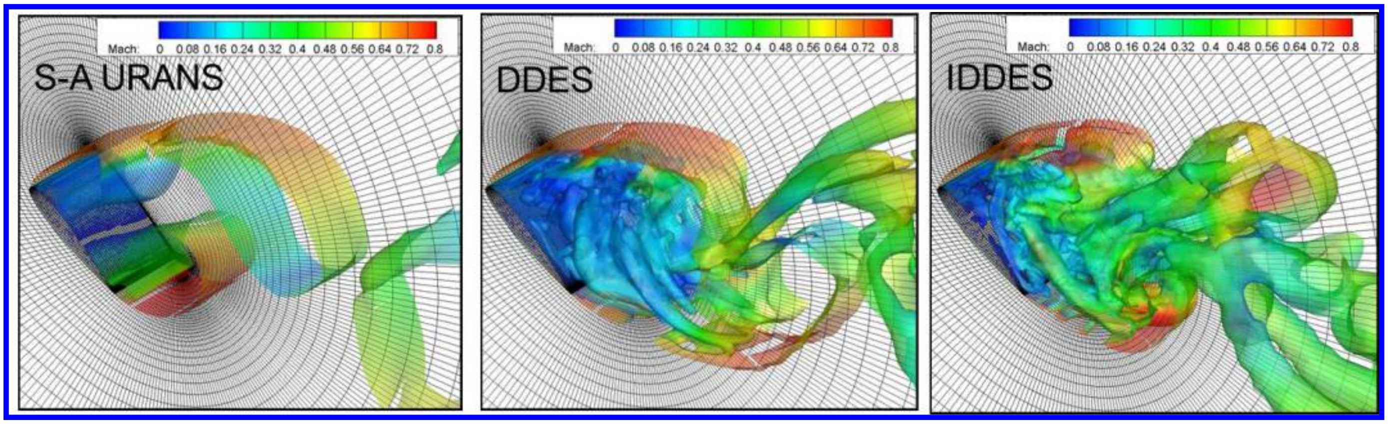

Figure 20: Iso-surfaces of the instantaneous Q-criterion=0, shown are the results of the S-A URANS, DDES and IDDES at AoA = 45°.

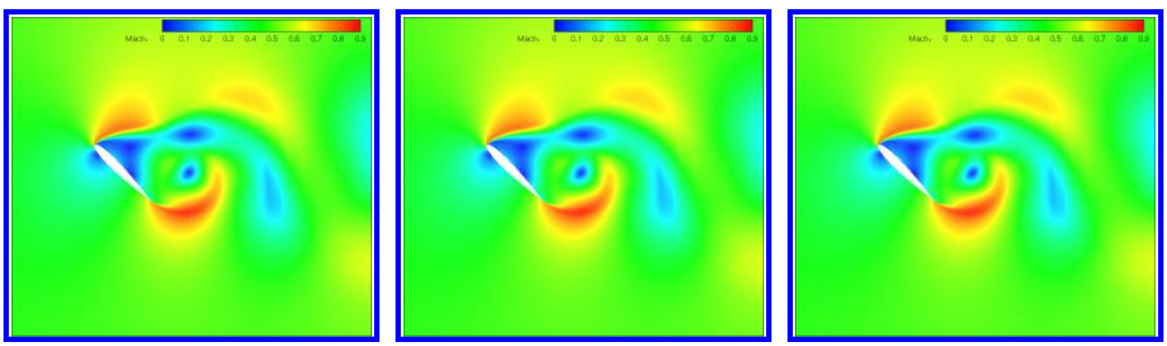

0.1Span 0.5Span 0.9Span

Figure 21: Mach contours at different spans in S-A URANS coarse mesh simulation at AoA = 45°

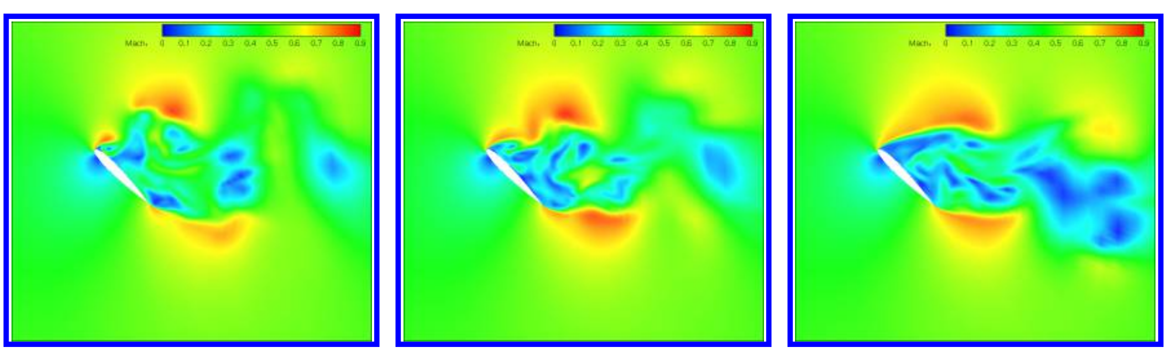

0.1Span 0.5Span 0.9Span

Figure 22: Mach number contours at three different spans in the IDDES coarse mesh simulation at AoA = 45°

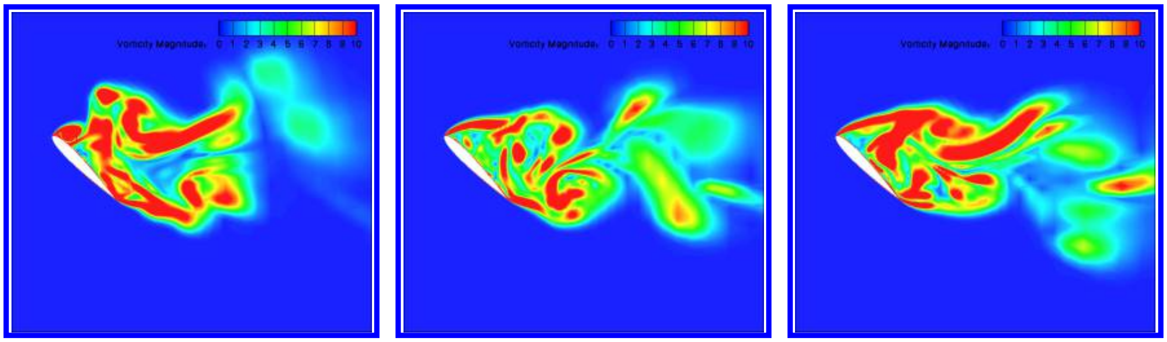

0.1Span 0.5Span 0.9Span

Figure 23: Vorticity contours at three different spans in the IDDES coarse mesh simulation at AoA $= 45°$

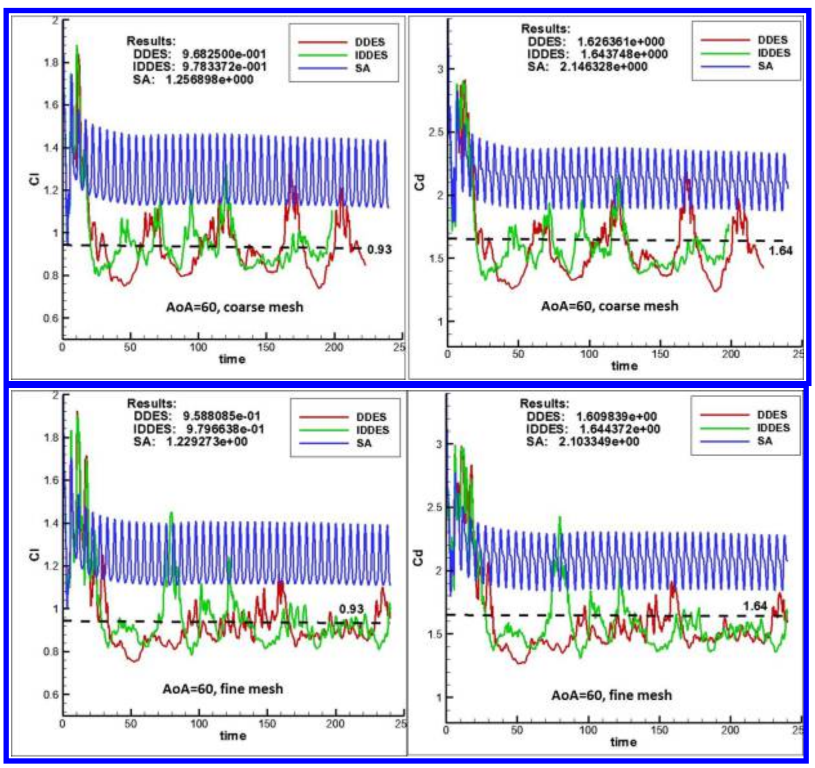

Figure 24: Lift and drag coefficient history at AoA $= 60°$.

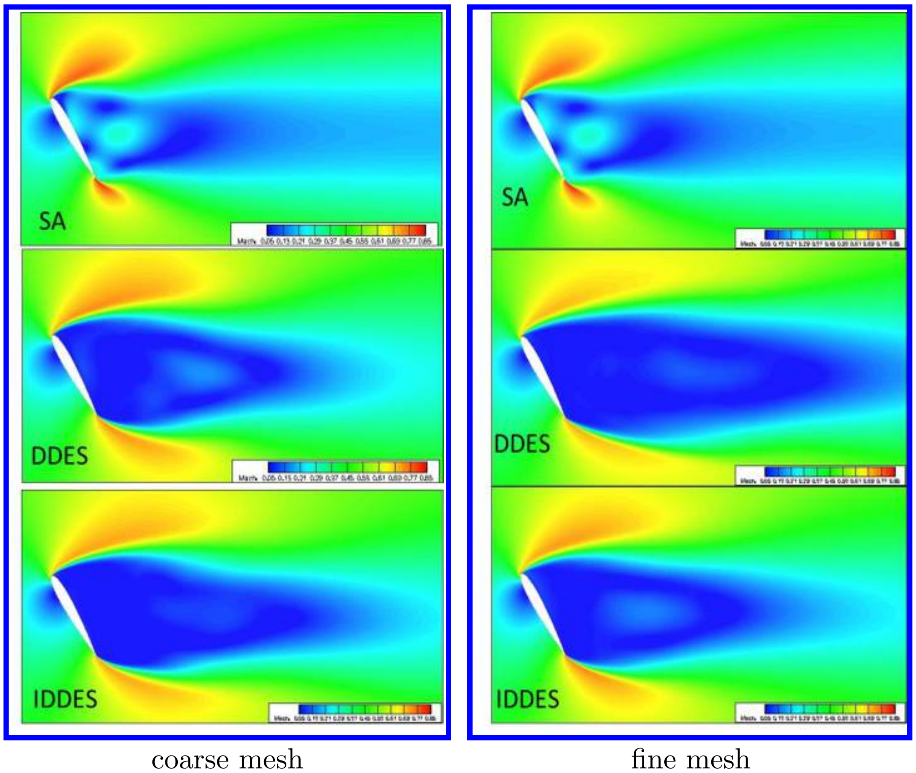

Figure 25: Time-averaged Mach contours at AoA = 60° in simulation with coarse(left) and fine(right) mesh.

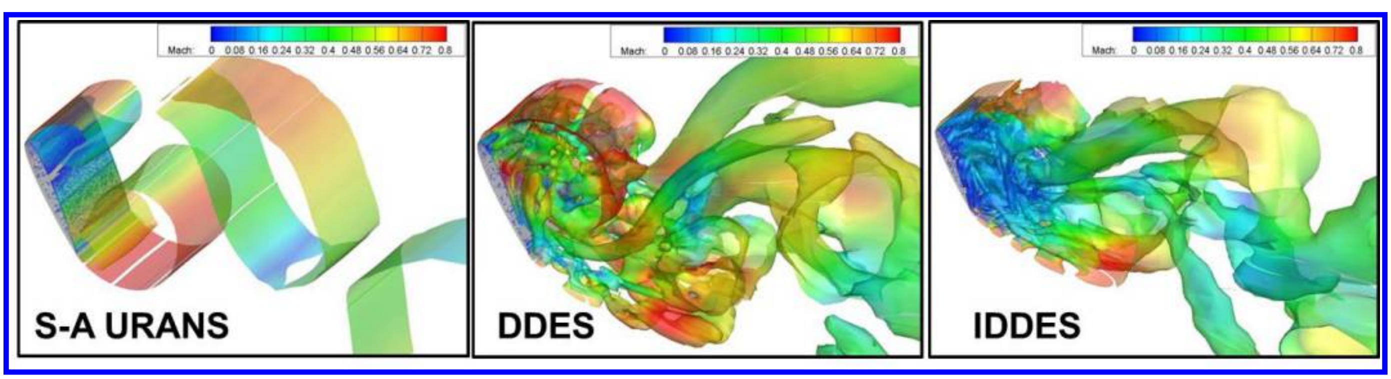

Figure 26: Iso-surfaces of the instantaneous Q-criterion=0, shown are the results of the S-A URANS, DDES and IDDES at AoA = 60°.